Journal of Polymer Research (2022) 29: 212
https://doi.org/10.1007/s10965-022-03045-y

ORIGINAL PAPER

PVDF-Fe_3O_4 nanocomposites: spectroscopic investigations

Dorina M. Chipara[1] · Alexandro Trevino[1] · Karen Lozano[2] · Bryan Hoke[1] · Karen S. Martirosyan[1] · Mircea Chipara[1]

Received: 13 October 2021 / Accepted: 22 April 2022 / Published online: 12 May 2022

Abstract
Nanocomposites have been prepared by melt mixing, loading the polyvinylidene fluoride matrix with various concentrations of magnetite. Wide Angle X-Ray Scattering, Raman, Fourier Transform Infrared, and Electron Paramagnetic Resonance spectroscopy were used to investigate these nanocomposites. Wide Angle X-Ray Scattering revealed that α is the dominant crystalline phase of the polymeric matrix irrespective of the loading with magnetite. Wide Angle X-Ray Scattering investigations on the dependence of the line positions and widths on the loading with magnetite are reported. Raman and Fourier Transform Infrared spectroscopy confirmed that the as-obtained nanocomposites consist of α polyvinylidene fluoride. The main Raman lines were identified, and the dependence of their parameters (line position and widths) on the loading by magnetite was reported. Raman and Wide Angle X-Ray Scattering data demonstrated a strong interaction between the matrix and the nanofiller. Electron Paramagnetic Resonance spectra of these nanocomposites reflect strong anisotropic electron interactions among the nanofiller's electrons.

Keywords Composite · Crystal · X-ray diffraction (XRD) · Electron paramagnetic resonance · Magnetic · Polymer · Raman and FTIR spectroscopy

Introduction

Polyvinylidene Fluoride (PVDF) is a thermoplastic polymer with a glass transition (labelled as β relaxation [1]) temperature ranging from –40 °C to –33 °C [2] or –28.6 °C [3] and a melting temperature in the range of 155–190 °C, depending on (crystalline) phase composition [4, 5]. PVDF is an amorphous-crystalline polymer characterized by a relatively large degree of crystallinity (typically over 50%). Up to five crystalline structures labeled α, β, γ, δ, and ε have been reported in PVDF [6]. The most frequently observed crystalline phase of PVDF is the α phase, which consists of a large series of CF_2-CH_2 monomers linked together in a (Trans)(Gauche)$^+$ (Trans)(Gauche)$^-$ nonpolar configuration [7, 8]. The unit cell of α PVDF (or form II PVDF) is monoclinic (a = 0.496 nm, b = 0.964 nm, c = 0.462 nm, and β* = 90°) [7, 8]. The β phase of PVDF has ferroelectric [9], piezoelectric [10, 11], and pyroelectric features. These features explain the efforts to obtain PVDF with higher β fractions. The unit cell of the β PVDF (or form I PVDF [8] is orthorhombic (a = 0.858 nm, b = 0.491 nm, and c = 0.256 nm) [8] with an all-trans zigzag planar configuration [7]. The γ phase of PVDF has a (Trans)(Gauche)(Trans)(Gauche)$^+$ (Trans)(Gauche)(Trans)(Gauche)$^-$ conformation [4], and it is monoclinic with a = 0.866 nm, b = 0.493 nm, c = 0.258 nm, and β = 97° [8].

The (almost) unique features of PVDF (ferroelectric [12], piezoelectric [13], and pyroelectric [12]), coupled with the low density, excellent stability to solvents, good flexibility [14], and good thermal stability [15] justifies the interest in PVDF based materials, and in particular on β phase PVDF. Potential applications include supercapacitors, batteries, flexible sensors [16], and nanogenerators [14] for the conversion of mechanical energy into electric energy. However, such features are demonstrated only by the β phase. Many experimental efforts aim to obtain a high fraction of β PVDF, thus enhancing the ferroelectric features.

The remaining δ and ε phases are rather exotic [4]. The main parameters determined from Wide Angle X-Ray Scattering (WAXS) are the line position, width,

✉ Mircea Chipara
mircea.chipara@utrgv.edu; chipara@yahoo.com

[1] Department of Physics, University of Texas Rio Grande Valley, 1201 W. University Drive, Edinburg, TX TX-78539, USA

[2] Department of Mechanical Engineering, University of Texas Rio Grande Valley, 1201 W. University Drive, Edinburg, TX TX-78539, USA

shape, and area or eventually relative intensity (usually defined by dividing the intensity of the given line by the intensity of the most intense line of the spectrum). The relative WAXS line's area is proportional to the number of reflections that contributed to that line. The width of each WAXS line is a convolution of two contributions: the extrinsic (instrumental, i.e., mostly errors) and the intrinsic (sample governed) contribution. Pending on the type of line shape, the experimental (as recorded) line width for a reflection along a direction perpendicular to the hkl plane, ω_{hkl}, is [17]:

$$\omega_{hkl} = \omega_{hkl}^{intrinsic} + \omega_{hkl}^{extrinsic} \quad (1)$$

$$\left(\omega_{hkl}\right)^2 = \left(\omega_{hkl}^{intrinsic}\right)^2 + \left(\omega_{hkl}^{extrinsic}\right)^2 \quad (2)$$

$$\left(\frac{\omega_{hkl}^{intrinsic}}{\omega_{hkl}}\right) = 1 - \left(\frac{\omega_{hkl}^{extrinsic}}{\omega_{hkl}}\right)^2 \quad (3)$$

where ω_{hkl} identifies the actual (measured) line width, $\omega_{hkl}^{intrinsic}$ represents the contribution to the line width due solely to the sample, and $\omega_{hkl}^{extrinsic}$ collects all the instrumental broadening contributions to the WAXS line. For a line width of both $\omega_{hkl}^{intrinsic}$ and $\omega_{hkl}^{extrinsic}$ described by Lorentzian line shape, the recorded line width is defined by Eq. (1). For a spectrum characterized by both Gaussian $\omega_{hkl}^{intrinsic}$ and $\omega_{hkl}^{extrinsic}$, the recorded line width is controlled by Eq. (2). Equation (3) describes the recorded line width as one component has a Lorentzian shape, and the other is Gaussian [17].

Raman investigations reveal the motions of small groups of atoms (stretching, bending, rocking, wagging) that involve a change in the polarizability of the sample. As in the WAXS experiments, the most important parameters of the Raman lines are the line position, width, shape, relative intensity, and relative areas. It was suggested by several authors [18, 19] that Raman spectra can provide a picture (and a better understanding) of the elastic features of materials at the molecular scale. The effect of strain on the Raman spectra was reported in several polymers (such as Kevlar fibers, where the Raman line located at 1610 cm^{-1} was reported to be displaced to smaller Raman shifts (by about 16 cm^{-1}) as the strain was increased by about 5%). The corresponding linewidth was broadened from 19 to about 28 cm^{-1} [20]. In polymer-based nanocomposites, the polymeric matrix tries to accommodate the filler by expanding its volume. This generates internal stresses and consequently is expected to affect the parameters of some Raman lines [18, 21, 22]. A study on the effect of a magnetic nanofiller (α - Fe_3O_4 or magnetite) on PVDF is reported.

Materials and methods

PVDF was purchased from Alfa Aesar as micron-sized powder. The nanofiller of choice was Fe_3O_4 with an average diameter of about 75 nm and black color, purchased from Nanostructured & Amorphous Materials, Inc. Both polymer and nanoparticles were used as received.

Sample's preparation Nanocomposites of PVDF- Fe_3O_4 containing various concentrations of Fe_3O_4 (0%, 0.2%, 0.6%, 1.2%, 2.4%, 5.8%, 12%, 23%, and 30% wt.) have been obtained by melt mixing using a Haake Polylab equipment with two counter-rotating screws. The three steps melt mixing started with an initial melt mixing at 190 °C and 60 rotations per minute (rpm) for 30 min, followed by a segment at 210 °C and 80 rpm for 15 min, and ended with a segment at 180 °C and 60 rpm for 30 min. Based on DSC data to be discussed in a subsequent manuscript, no degradation of the polymeric matrix was noticed. Before each measurement, the samples were heated at 190 °C for about 10 min and then cooled down slowly to room temperature (in about 30 min). DSC heating/cooling cycles confirmed that the samples were free of any residual stress. The relatively high mixing temperature(s) and long mixing time(s) were selected to achieve the conversion of the nonpolar α phase into the polar β phase [23].

Experimental techniques The obtained nanocomposites were investigated by various techniques. Wide Angle X-Ray Scattering (WAXS) investigations were performed with a Bruker Discovery 8 system, Raman spectroscopy analysis was performed by using a Renishaw InVia confocal microscope, equipped with a laser operating at 785 nm, FTIR measurements were performed using Bruker Hyperion Confocal Microscopy, and Electron Paramagnetic Resonance investigations were done by using as Elexsys Bruker spectrometer operating in the X Band.

Results

WAXS spectra of the as-obtained nanocomposites are shown in Fig. 1. The top panel includes low reflection angles, and the lower panel collects larger reflection angles. Both graphs have the reflections labeled for the polymeric matrix (online appears in blue) and the nanofiller (online appears in red) and indexed. It is noticed that the top panel of Fig. 1 includes only reflections that involve the polymeric matrix, and in particular, the α phase of PVDF. Within experimental errors, no other phases of PVDF were observed. It was noticed that as the Fe_3O_4

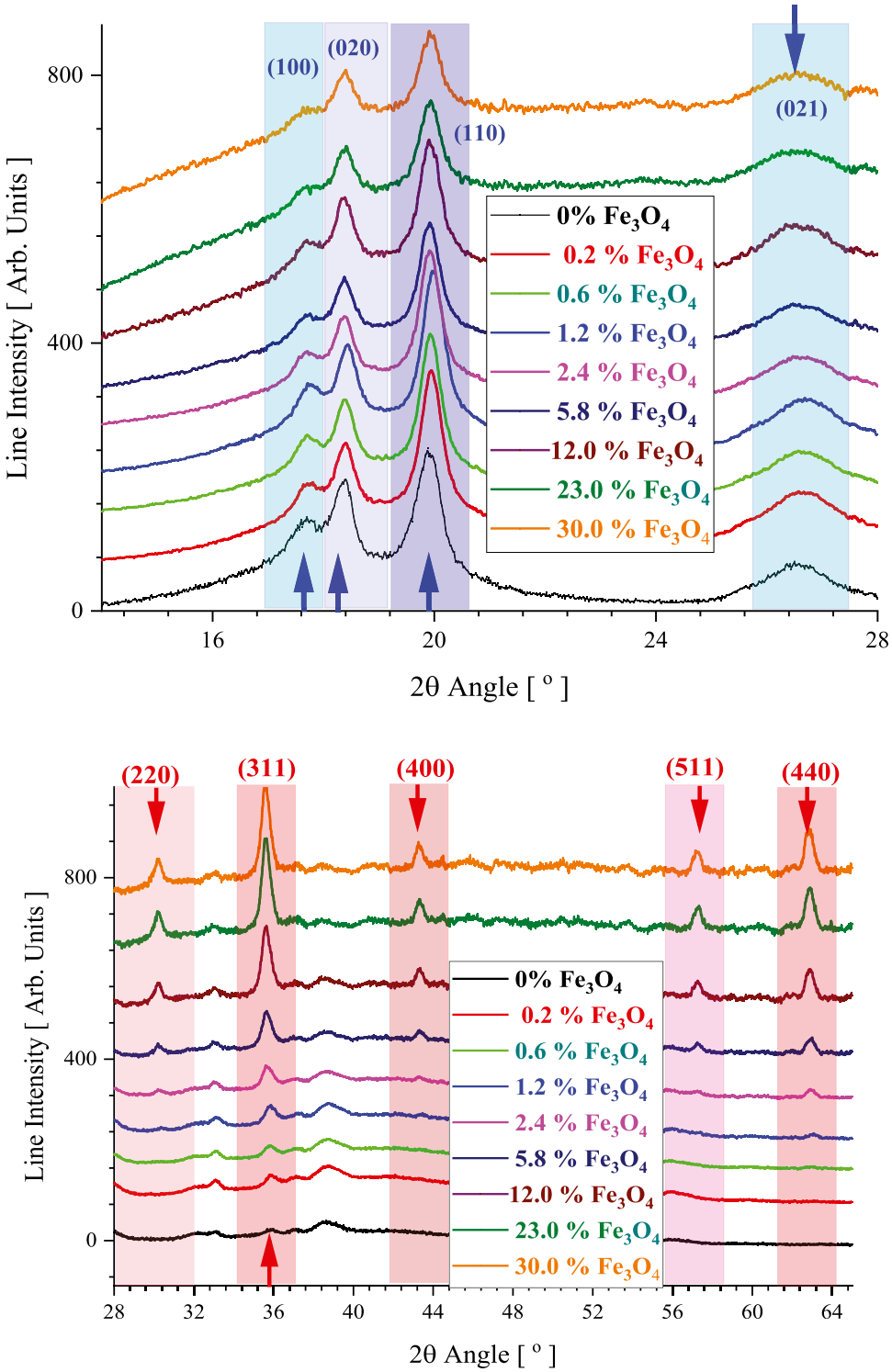

Fig. 1 WAXS spectra of PVDF-Fe3O4 nanocomposites for low reflection angles (top panel) and large reflection angles (low panel)

content was increased, the lines assigned to the polymeric matrix became weaker, suggesting a decrease in the degree of crystallinity of the polymeric matrix due to the addition of the nanofiller.

The lower panel of Fig. 1 includes larger angles of reflections and collects mainly the lines due to the nanofiller. The first four reflections located at about 17.6°, 18.4°, 19.9°, and 27.0° are assigned to the (100), (020), (110), and respectively (021) reflections originating from the monoclinic unit cell of the α PVDF phase [16, 22, 24]. The line corresponding to the (120) reflection was [25] not observed. The actual reflections showed weak

displacements from the theoretical values calculated for an unit cell with a = 4.96 Å, b = 9.64 Å, c = 4.62 Å, β* = 90° [16, 24]. The analysis of the as-recorded experimental diffractograms was performed using the Origin C programming and graphical capabilities, assuming that each line is described by a single Lorentzian. The first three reflections located at about 17.6°, 18.4°, and 19.9° (which are the most intense lines of these spectra) were assigned to the (100), (020), and respectively (110) reflections originating from the α PVDF phase [22] and were fitted together by a superposition of 3 Lorentzian like line shapes, using the expression:

$$\begin{aligned} I(x) = {} & (2*A_1/\pi)*(W_1/(4*(x - C_1) + W_1*W_1)) \\ & + (2*A_2/\pi)*(W_2/(4*(x - C_2)*(x - C_2) + W_2*W_2)) \\ & + (2*A_3/\pi)*(W_3/(4*(x - C_3)*(x - C_3) + W_3*W_3)) \\ & + B + S*x + Q*x*x; \end{aligned} \tag{4}$$

where x is the current reflection angle (2 thetas, in degrees), I is the intensity of the as-recorded spectrum, A_1, A_2, and A_3 are the individual intensities of each line, C_1, C_2, and C_3 denote the position (peak) of each reflection, W_1, W_2, and W_3 are the width of the three reflections, B is the base correction, S is the slope correction, and Q is the quadratic corrections (for all these three lines). The next line representing the (021) reflection of α PVDF was fitted separately by using the expression for Lorentzian lines:

$$\begin{aligned} I = {} & (2*A/\pi)*(W_1/(4*(x - C_1)*(x - C_1) + W_1*W_1)) \\ & + B + S*x + Q*x*x; \end{aligned} \tag{5}$$

where I is the intensity of the as-recorded spectrum, A is the intensity, C is the position of the (021) reflection, and W is the width of this reflection. B, S, and Q have the same significance as in Eq. (4).

From Figs. 2 and 3, it is noticed that the Eqs. (4) and respectively (5) provide an excellent fitting of the experimental data; here, the symbols represent actual data points, and the (red) line corresponds to the best fitting. It is concluded that the best fit of WAXS lines is consistent with Lorentzian shapes; accordingly, the as recorded line width (for all lines) is described by Eq. (1) [17]. All fitted spectra were characterized by correlation coefficients better than 0.97, as a very large number of data points (of the order of 10^2) are involved in the fit of any WAXS reflection.

The dependence of the line position (in 2θ) on the loading with Fe_3O_4 for the first four reflections assigned to α PVDF is shown in the top graph of Fig. 4. As the concentration of nanofiller is increased from 0 towards 1.2% wt. Fe_3O_4, the positions of all four lines assigned to the polymeric matrix are shifted towards larger angles. Hence, in this range of nanofiller concentrations, the size of the unit cell assigned to the polymer (along directions perpendicular to the planes discussed) is shrinking as the Fe_3O_4 concentration is increased. It is suggested that for such concentrations the nanofiller is accommodated through the elastic features of the matrix. Hence, the increase of the nanofiller's concentration will enhance the pressure exerted on the polymeric crystal unit cell. However, as the concentration of Fe_3O_4 is further increased (towards 6% wt. nanofiller), the size of the unit cell starts to grow (the position shifts to smaller angles). These changes indicate that the enhanced loading with Fe_3O_4 generates significant stress within the bicontinuous amorphous phase of PVDF, to increase the size of crystallites by crystallization under stress. Eventually, some amorphous domains may be fractured, releasing some of the local pressure exerted on polymeric crystal and allowing for a recovery towards the initial size of the unit cell. For Fe_3O_4 concentrations above 6% wt., the positions of these four lines are almost independent of the content of the nanofiller, thus suggesting that the nanofiller broke the bicontinuous amorphous PVDF phase and started eventually to bleed from the nanocomposite through the amorphous regions, resulting in the relaxation of stresses/strains exerted on crystalline domains.

The middle graph of Fig. 4 represents the dependence of the line widths associated with the (100), (020), (110), and respectively (021) reflections on the loading with iron oxide. The dependence of the widths of these lines on the loading with Fe_3O_4 exhibits the same three-domain structure as for the positions of these lines. As the concentration of Fe_3O_4 is increased from zero towards 0.6% wt. Fe_3O_4, the linewidths are decreasing, supporting an increase in the size of crystallites.

Further addition of nanofiller up to 1.2% wt. Fe_3O_4 results in a domain where the increase of the nanofiller's concentration increases the linewidth. Higher concentrations of nanofiller do not produce significant modifications on the line widths. It is suggested, based on the lower density of amorphous polymers (compared to the density of the crystalline ones), that the nanofiller is preferentially trapped within the amorphous domains. The lowest graph in Fig. 4 magnifies this dependence for low concentrations of nanofiller.

The (021) reflection has a different behavior, suggesting that the dominant distortion of the unit cell due to the nanofiller is along a direction perpendicular to the plane (021). The main difference between the line position and line width is that the line position is related to the dimensions of the unit cell. In contrast, the line width is dominated by the crystallites' features (i.e., is affected by crystallites size and by the stress and strain acting on crystallites).

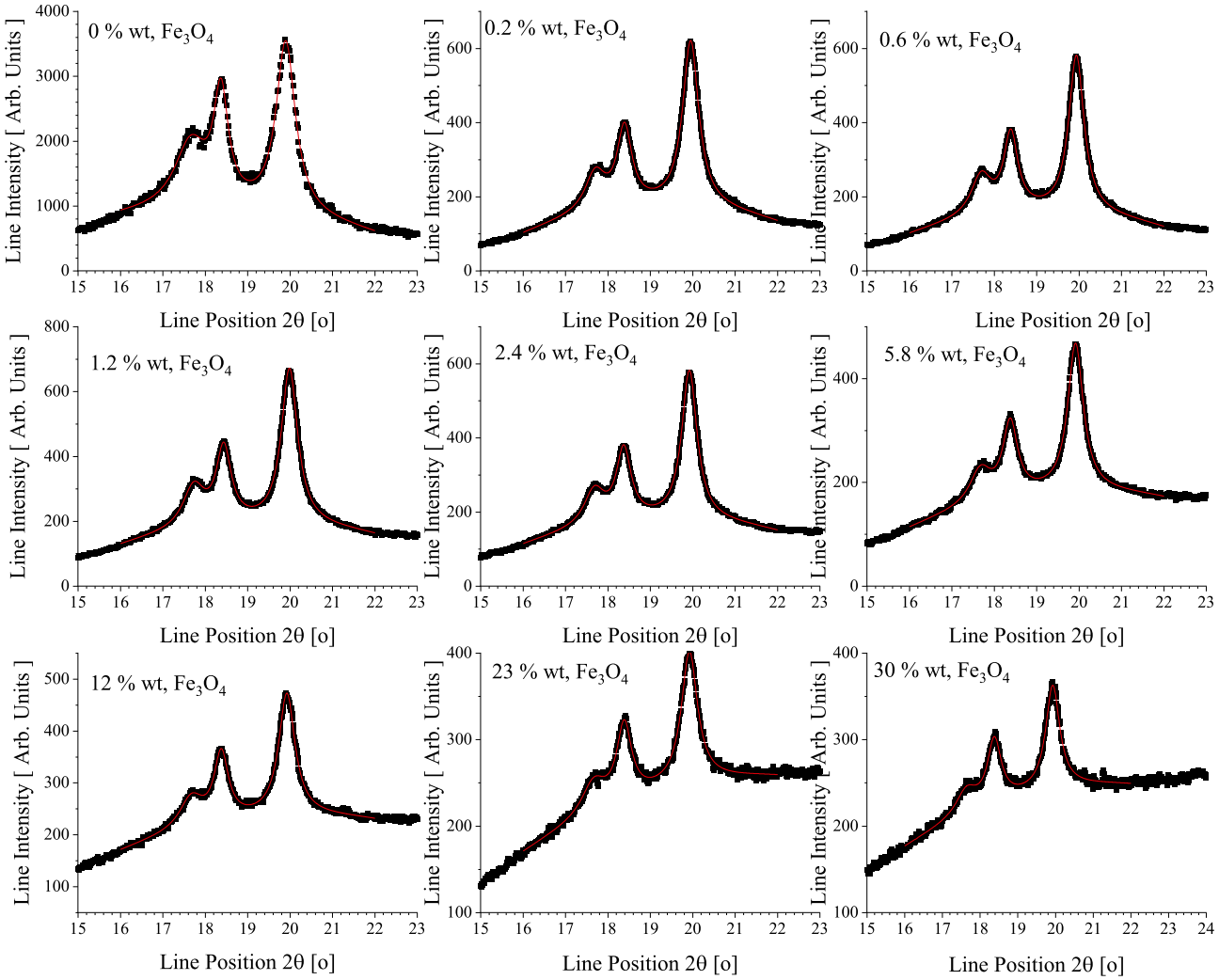

Fig. 2 WAXS spectra of the first three lines assigned to αPVDF. The black symbols represent the actual experimental data and the red line is obtained by using the best fit parameters using Eq. (4)

Several scenarios will be considered to analyze the dependence of linewidth on the loading with nanoparticles:

1. The line width is controlled by the size of crystallites.

   Assuming that the dependence of the line width on the loading by iron oxide is controlled by the size of α-PVDF crystallites, $D_{hkl,}$ the Scherrer equation predicts

$$D_{hkl} = \frac{K\lambda}{w_{hkl}\cos\theta_{hkl}} \tag{6}$$

   where λ is the wavelength of the incident X-Ray, K is a constant (that depends on the crystallites symmetry), θ_{hkl} is the diffraction angle for the plan characterized by the Miller indices h, k, and l, D_{hkl} is the length of the crystallite along a direction perpendicular to hkl plane, and w_{hkl} is the width of the corresponding line. Some authors consider D_{hkl} as being an averaged quantity and therefore to exhibit no dependence on the indices h, k, l (or on the reflection order) [26].

Figure 5 collects the dependence of the length of α-PVDF crystallites (Scherrer crystalline size) along some crystalline directions (as estimated using Eq. 6) on the loading with Fe_3O_4. It is noticed that the estimated Scherrer length of α-PVDF along the directions perpendicular to the (100), (021), and (110) planes increases as the loading with Fe_3O_4 is increased. Within this model, the linewidth is broadened, and the size of crystallites is rapidly growing as the loading by Fe_3O_4 is increased from zero to about 0.6% wt. Fe_3O_4. This may reflect the crystallization growth/nucleation under stress- a feature that is well documented for polymeric materials and polymer-based nanocomposites [27–29]. Further increase of the nanofiller content towards 1.2% wt. Fe_3O_4 results in a weak decrease of the polymeric crystallites' size

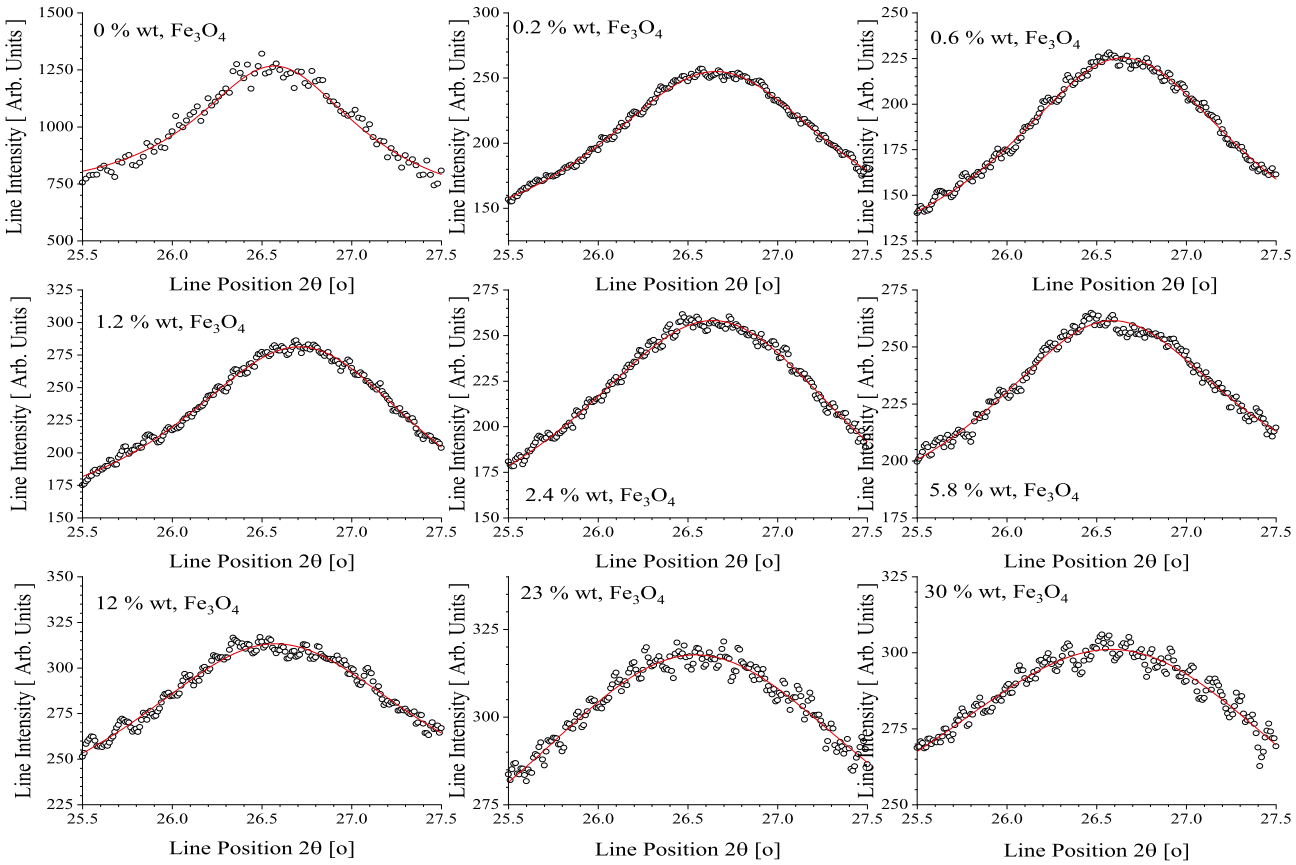

Fig. 3 WAXS spectra of the line observed at 2θ = 26.5° assigned to αPVDF. The black symbols represent the actual experimental data and the red line is obtained by using the best fit parameters, using Eq. (5)

eventually reflecting a weak relaxation due to the generated extra volume by the increase of the size of crystallites. Higher concentrations of Fe_3O_4 produced an increase in the size of crystallite domains as the loading with nanofiller was increased. A plateau of the crystallite size dependence on the loading by Fe_3O_4 was noticed above 5.8% Fe_3O_4. The Scherrer length along the direction perpendicular to the 021 planes has an opposite dependence of Fe_3O_4 concentration (decreases as the Fe_3O_4 content is increased). This may eventually reflect a Poisson effect [11] due to the stretching of polymeric crystallites (along the directions perpendicular on the (100), (021), and (110) planes).

2. The line width is controlled by the strain.

Assigning all these changes of the line width to strain along a direction perpendicular to hkl plane, ε_{hkl}, the Wilson expression [30, 31] connects the line width to the strain by the equation

$$\varepsilon_{hkl} = \frac{w_{hkl}}{4\tan\theta_{hkl}} \tag{7}$$

where w_{hkl} is the line width for the reflection perpendicular to the hkl plane and θ_{hkl} represents the corresponding diffraction angle. Figure 6 depicts the dependence of the Wilson strain, as calculated according to Eq. (7) (i.e., assuming that the linewidth is controlled solely by the strain) on the Fe_3O_4 loading. It is easily noticed that as the concentration of nanofiller is increased from 0 to about 1% wt. Fe_3O_4, the strain within the nanocomposite is decreasing, suggesting a certain relaxation of the polymeric matrix. Further loading with nanofiller results in the expected increase of the Wilson line width as the loading by Fe_3O_4 is increased. This dependence is small for the directions perpendicular to the planes (100) and (020), medium for the plane perpendicular to the (110) direction, and large for the direction perpendicular to the (021) plane.

3. The line width is controlled by both the size of crystallites and strain/stress.

For such an analysis, the quantity $w_{hkl}\cos\theta_{hkl}$ plays a significant role because the competition between crystallite size and strain may be expressed as a linear com-

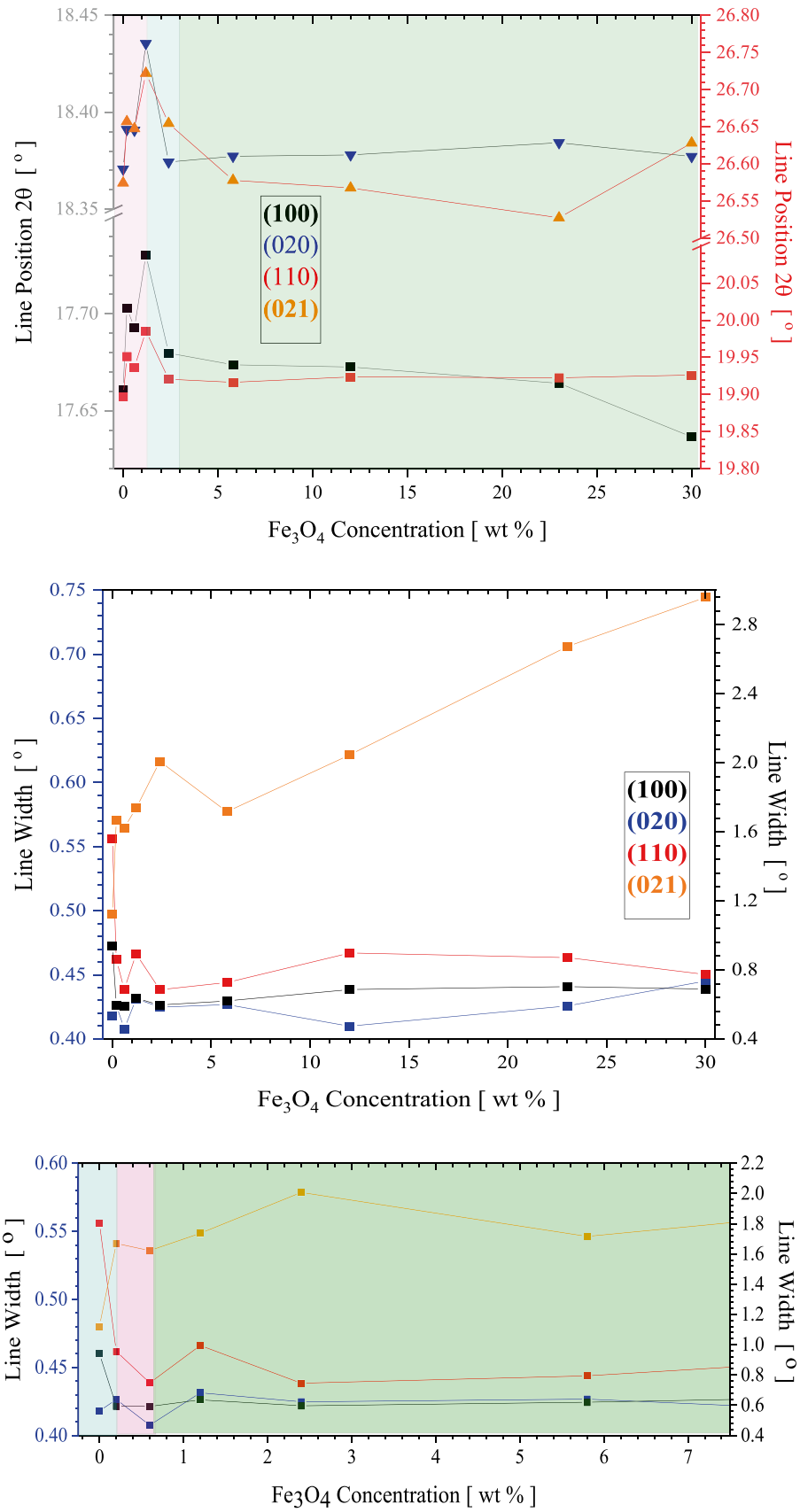

Fig. 4 The dependence of the line position and line width on the loading by Fe_3O_4 for the first four reflections assigned to a PVDF

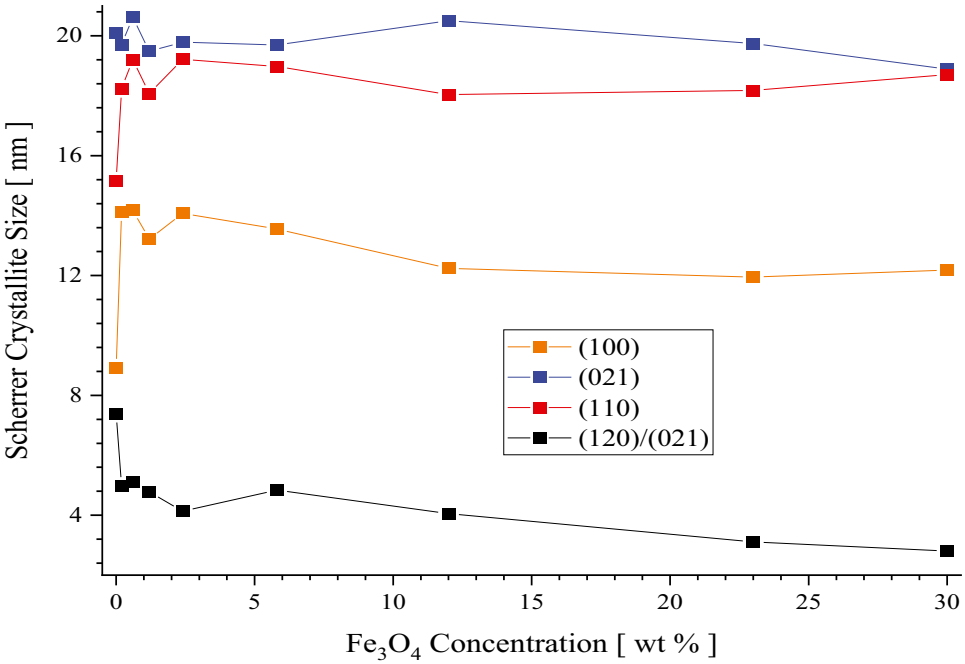

Fig. 5 The dependence of the PVDF crystallites length L_{hkl} directions perpendicular on the planes hkl as predicted by Scherrer (Eq. 6) for various loading with Fe_3O_4

bination (Williamson Hall approximation) [30–32], of these contributions:

$$w_{hkl}\cos\theta_{hkl} = \frac{K\lambda}{D_{hkl}} + 4\,\varepsilon_{hkl}\sin\theta_{hkl} \tag{8}$$

By defining $y = w_{hkl}\cos\theta_{hkl}$ and $x = \sin\theta_{hkl}$, the equation will be transformed into the equation of a straight line ($y = K\lambda/D_{hkl} + 4\varepsilon_{hkl}x$), which passes through $K\lambda/D_{hkl}$ and has a slope $m = 4\varepsilon_{hkl.}$ In the general case, the Eq. (8) may be rewritten as:

$$w_{hkl}\cos\theta_{hkl} = \frac{K\lambda}{D_{hkl}} + F\sin\theta_{hkl} \tag{9}$$

where $F = 4\varepsilon_{hkl}$ for the WH isotropic strain model [30], and $F = 4\sigma/E_{hkl}$ or $F = (2^{5/2}E_{hkl}{}^{-1/2})u^{1/2}$ for the WH anisotropic strain model [30, 33] where E_{hkl} represents

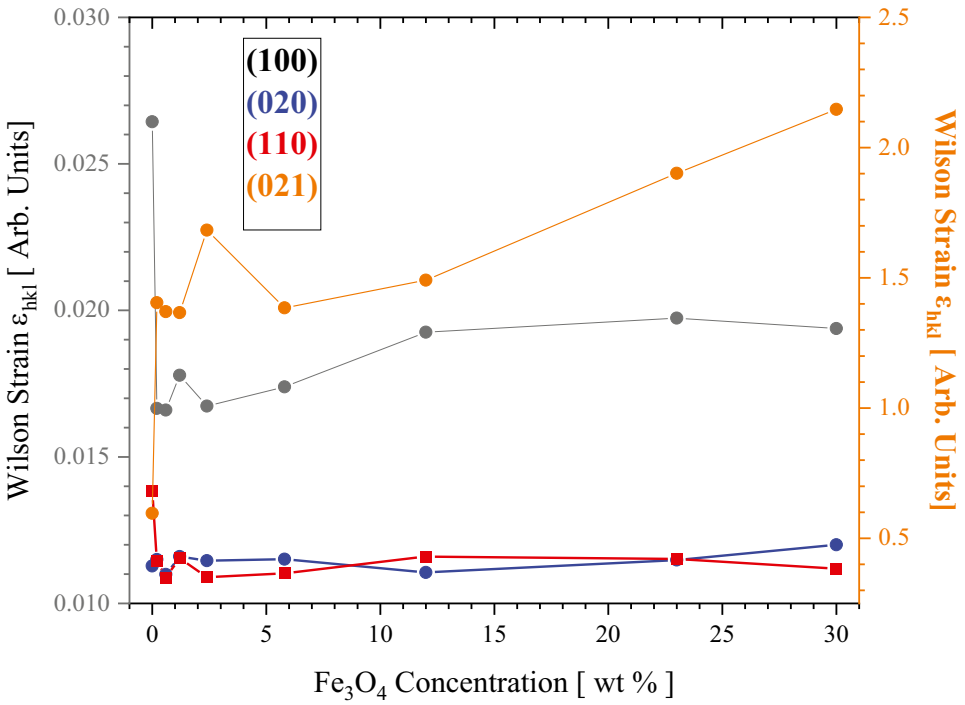

Fig. 6 The dependence of the Wilson strain, estimated using Eq. (7) (assuming that this is the dominant line broadening process) for various reflections of the PVDF crystallites as a function of Fe_3O_4 loading

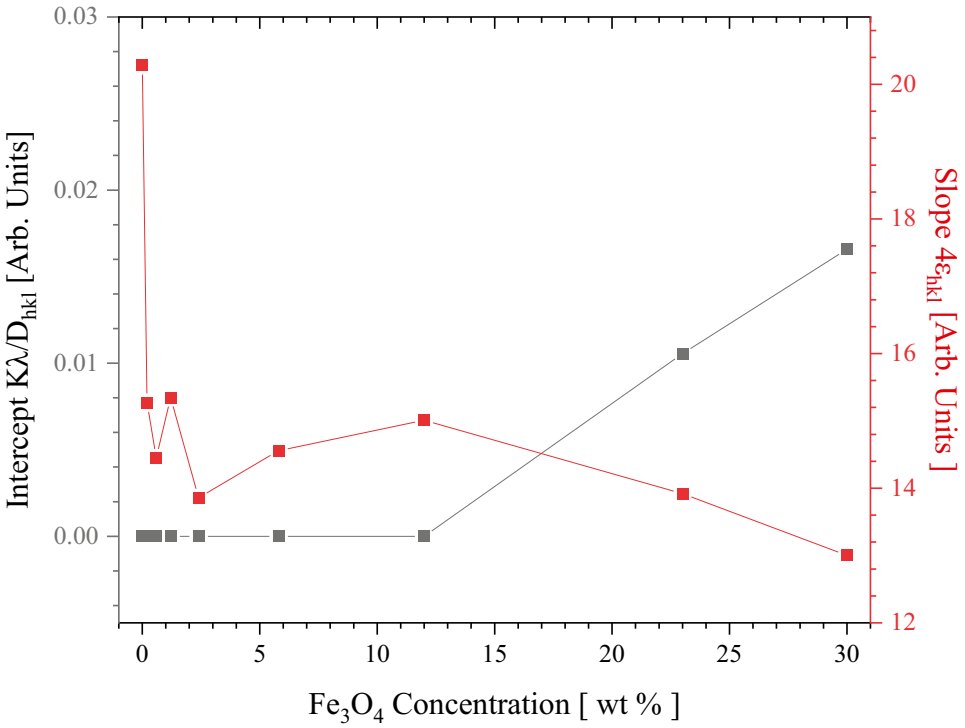

Fig. 7 The slope and intercept contributions to the line width of the α-PVDF

the projection of the Young modulus along directions perpendicular to the hkl planes, and u represents the energy per unit volume as expressed by Hooke's law: $u=(E_{hkl}\varepsilon^2_{hkl})/2$ [30, 33].

The actual dependence of $w_{hkl}\cos\theta_{hkl}$ on $\sin\theta_{hkl}$ does not describe very nicely the experimental data suggesting additional contributions, eventually originating from the polymer-nanofiller interface as well as from the departure of the lines from a pure Lorentzian. However, the main conclusion derived from Fig. 7 is that the crystallite size dominates the behavior of the line width for concentrations below 10% wt. Fe_3O_4, while for higher concentrations of nanofiller both the crystallite size and the strain are competing in affecting the line width.

A single line originating from the nanofiller can be analyzed in detail (see the left panel of Fig. 8). This line, located at about 35.7° has been identified as representing the (311) reflection and has been reported as the most intense line of

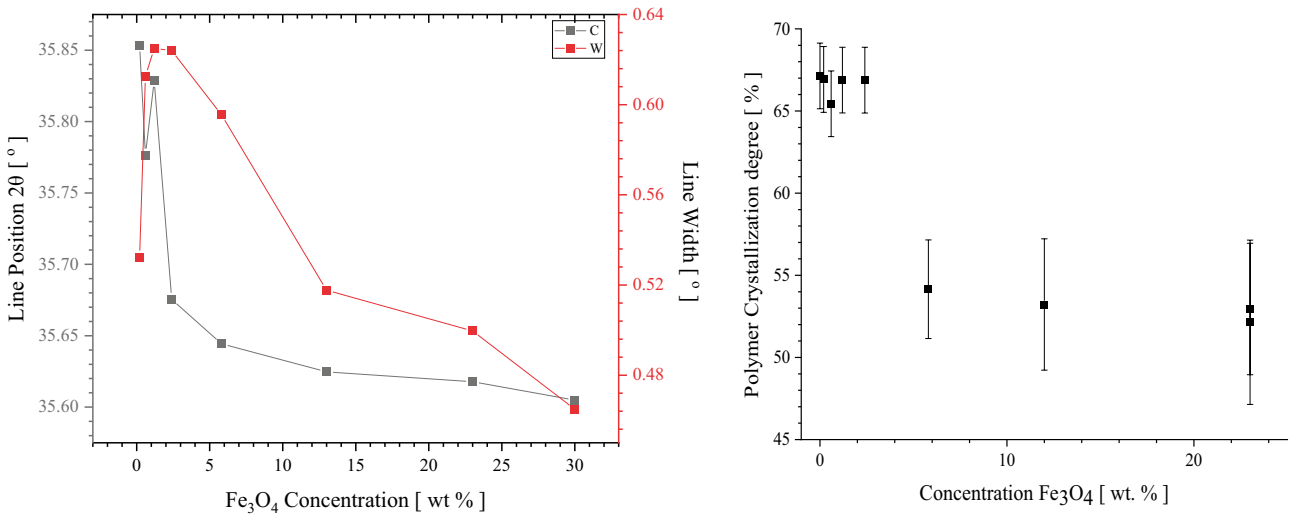

Fig. 8 Left: The dependence of line position and line width for the WAXS line located at 35.7° assigned to Fe_3O_4 on the loading with nanofiller. Right: The dependence of the polymer degree of crystallinity on the loading with PVDF (as determined from the areas of WAXS spectra)

Fe_3O_4 nanoparticles [34]. The dependence of line position and line width on the Fe_3O_4 loading (for the line located at $2\theta = 35.7°$) indicates that as the Fe_3O_4 concentration is increased above 1.0%wt, both the line width and the line position are decreasing. This indicates a slight dilation of the unit cell of the Fe_3O_4 coupled with an increase in the size of crystallites, probably due to the coalescence of magnetic nanoparticles within the polymeric matrix. To conclude, the WAXS line of the nanofiller is controlled by the size of crystallites, which is increasing due to the coalescence of nanoparticles controlled by the attraction among magnetic nanoparticles.

The right panel of Fig. 8 represents the dependence of the degree of crystallinity for the polymer, as a function of the Fe_3O_4 wt. loading. For the samples loaded by less than 5.5% weight Fe_3O_4, the degree of crystallinity is oscillating within experimental errors. Larger loading concentrations produce a strong drop in the degree of crystallinity.

The Raman spectra ranging from 100 to 2600 cm^{-1} are shown in Fig. 9, where the most important Raman lines originating from the polymeric matrix are identified and assigned. All PVDF lines observed in the PVDF-Fe_3O_4 nanocomposites were assigned to the α-PVDF phase.

The Raman lines of the nanofiller (Fe_3O_4) are not easily noticed as they are weak and broadened by the interaction with the polymeric matrix. The most intense Raman line of Fe_3O_4 was noticed at about 713 cm^{-1} (compared to 710 cm^{-1} reported in the literature [34]) and identified as representing the A_{1g} mode [34].

All Raman lines assigned to PVDF are gradually decreasing in intensity and broadening (and finally disappear) as the concentration of the iron oxide is increased. The dependence of the line position and linewidth of some of the most intense and isolated Raman lines has been analyzed in more detail. To achieve this goal, these lines were isolated and fitted assuming a single Lorentzian line shape (see Eq. 1).

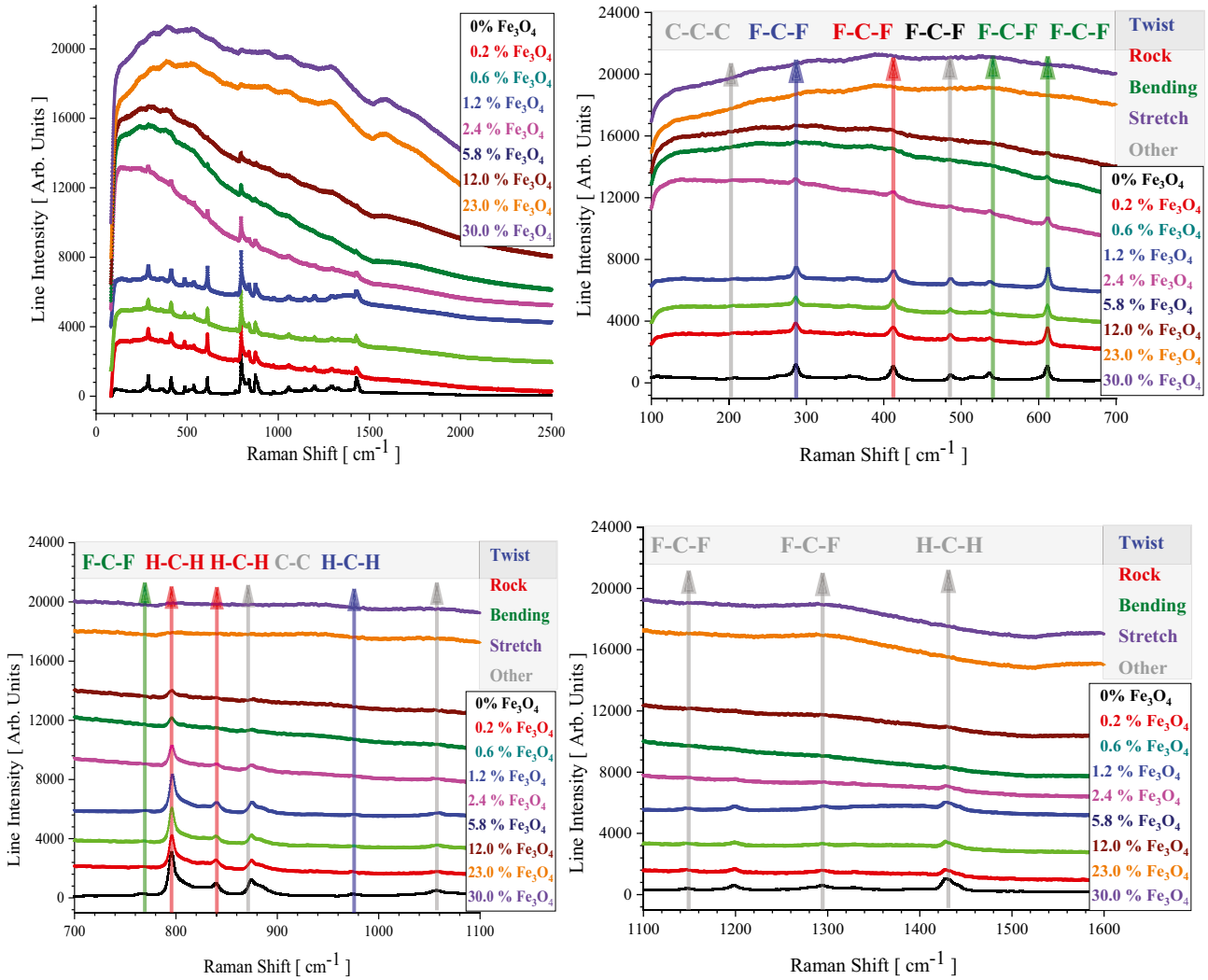

Fig. 9 Raman spectra of PVDF-Fe_3O_4 nanoparticles

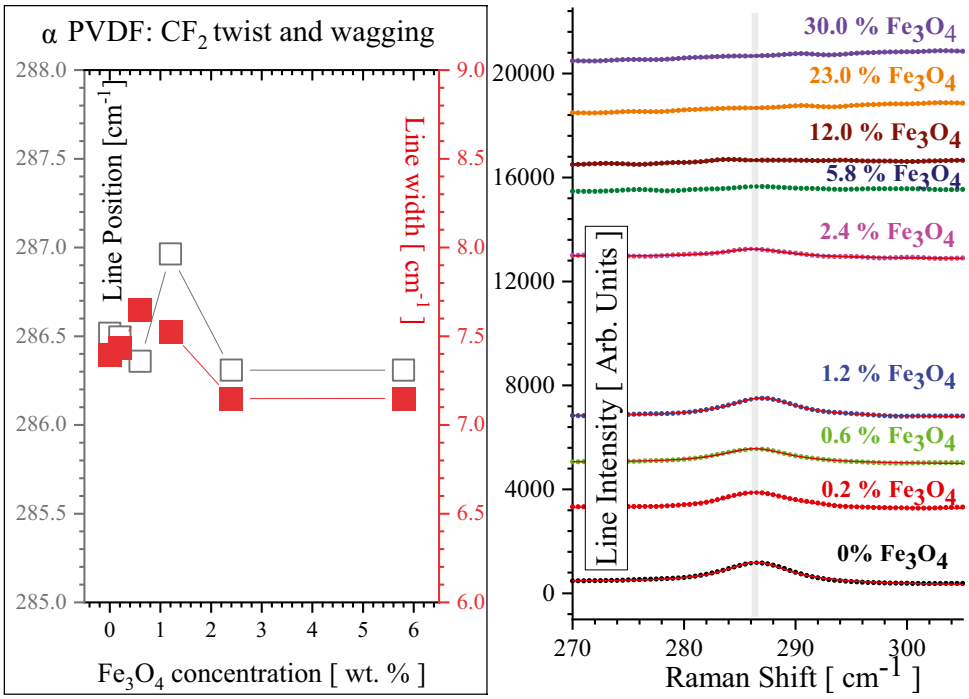

Fig. 10 Left: The dependence of the line position and line width for the Raman line located at 285 cm^{-1}. Right: Raman symbols identify Raman data while the red lines identify the best fit for shifts ranging from 270 to 305 cm^{-1} and various loading with the nanofiller

This fit was typically excellent, and the dependence of the most important parameters (line position and line width) was monitored for different loadings with Fe_3O_4. Figure 10 shows on the right panel the actual Raman spectra (colored symbols) as well the best fit (red lines), while the left panel shows the dependence of the line position and line width (determined from the best fit) on the loading with Fe_3O_4. At low concentrations of nanofiller (below 1% wt.), the line position is shifted to larger Raman shifts, while the Raman line is broadened. In the range of 1% wt. Fe_3O_4 to 2% wt. Fe_3O_4, the Raman parameters relaxed to values close to the initial one. Larger loading with Fe_3O_4 does not affect these parameters (position and width). This line was assigned to CF_2 twist and wagging [22]. This Raman line was reported at 284 cm^{-1}, with a line width of about 9 cm^{-1}, and assigned to CF_2 twisting and wagging in α-PVDF [7]. The 4 × stretching of the PVDF sample resulted in a decrease in line intensity, a shift of the position to 276 cm^{-1}, and a narrowing of this line to about 4 cm^{-1} [7].

The right panel of Fig. 11 shows the actual Raman spectra (colored symbols) as well the best fit (red lines) for a significant narrow window of Raman shifts, while the left panel shows the dependence of the line position and line width (determined from the best fit) on the loading with Fe_3O_4. Discrepancies between the dependence of the Raman line position and width on the loading with Fe_3O_4 for Raman lines occurring at different positions are noticed. These discrepancies reveal the complex nature of the Raman spectra. For example, the Raman line located at 611 cm^{-1} is identified as originating from a more complex molecular set of motions that includes CF_2 bending and wagging as well as CCC scissoring [22]. It is suggested that the modified dependence at large loading with Fe_3O_4 reflects the CCC scissoring that involves a larger volume of the polymer, including the C-C backbone. This is an excellent example showing the effect of molecular architecture on the properties of polymers. This line was also reported at 609 cm^{-1}, characterized by a line width of about 4 cm^{-1}, and assigned to CF_2 and CCC scissoring in α PVDF [7]. Upon 4 × stretching, the line was reported [7] to shift towards 602 cm^{-1}, broaden to 22 cm^{-1} and decrease in intensity.

The line observed at 796 cm^{-1} was reported [7] as the most intense line of the α-PVDF, located at 794 cm^{-1}, characterized by a width of 8 cm^{-1}, and assigned to CH_2 rocking. Figure 12 presents the dependence of the line position and linewidth for the Raman line located at 796 cm^{-1}. It was reported that upon the 4 × stretching, the position of this line moved to 796 cm^{-1}; the line broadened to about 22 cm^{-1}, and its intensity decreased dramatically [7]. It was also reported [35] that the increase of the estimated draw ratio from 1.4 to 4.0 results in a substantial decrease in the intensity and width of this line, including a small displacement of the position of this line to larger shifts (cm^{-1}) [35].

FTIR and Raman are complementary experimental techniques, both focused on the absorption of electromagnetic radiation (in the range of 0 to 4000 cm^{-1}). Some absorption (emission) lines were noticed both in Raman and FTIR spectra while some lines are specific either to Raman or to FTIR. The main difference derives from the fact that this absorption/emission of electromagnetic radiation in FTIR

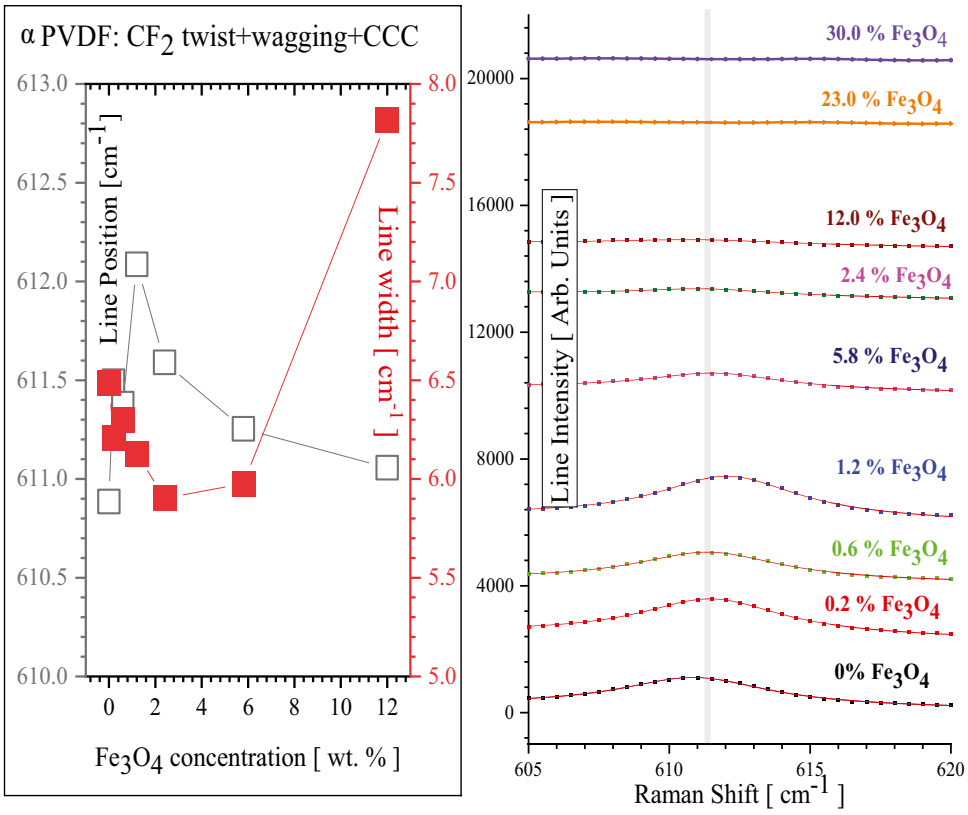

Fig. 11 Left: The dependence of the line position and line width for the Raman line located at 611 cm^{-1}. Right: Raman symbols identify Raman data while the red lines identify the best fit for shifts ranging from 605 to 620 cm^{-1} and various loading with the nanofiller

is associated with a change of the dipole moment, while Raman spectroscopy requires a change of the polarizability. FTIR spectrum of PVDF loaded by Fe_3O_4 is shown in the top panel of Fig. 13A.

The FTIR spectrum of PVDF – Fe_3O_4 nanocomposites is complex; the overlap between the lines due to the polymeric matrix with the lines originating from the nanofiller makes it difficult for quantitative analysis. Detailed spectra for the

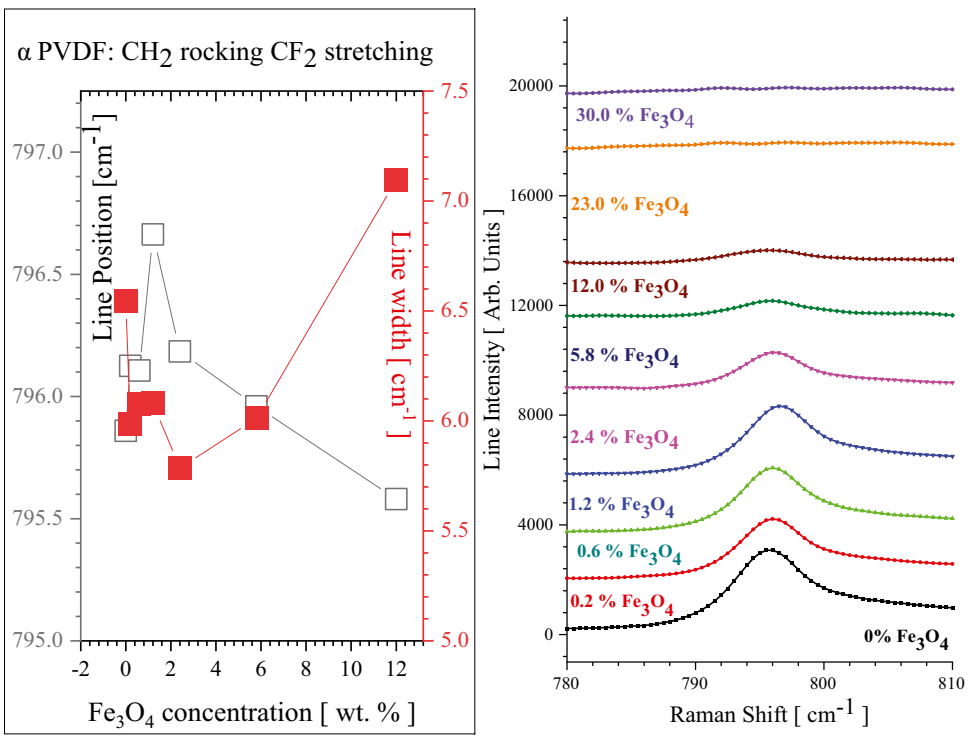

Fig. 12 Left: The dependence of the line position and line width for the Raman line located at 796 cm^{-1}. Right: Raman symbols identify Raman data while the red lines identify the best fit for shifts ranging from 780 to 810 cm^{-1} and various loading with the nanofiller

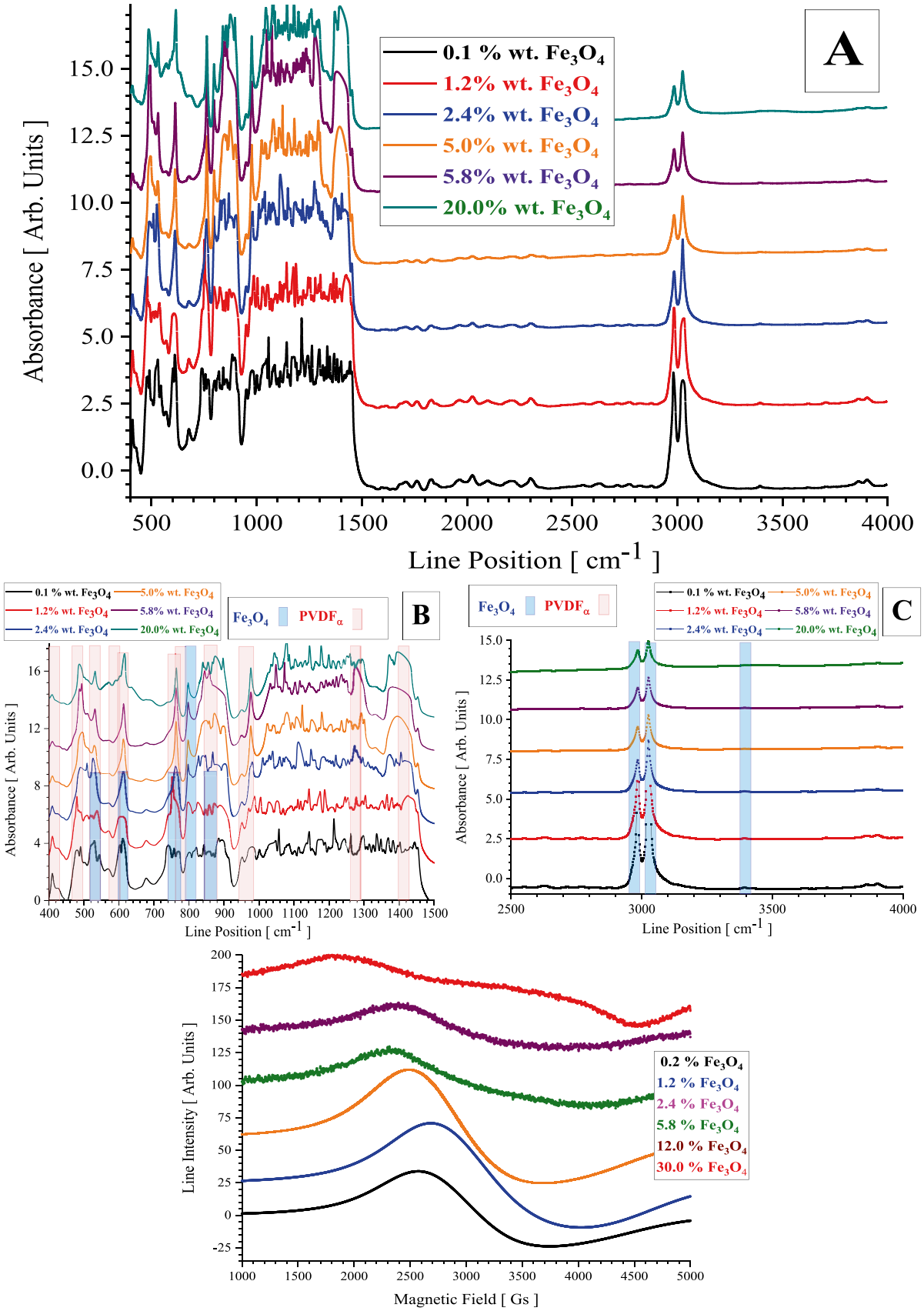

Fig. 13 **A**, **B**, and **C**. FTIR spectra of PVDF-Fe_3O_4 nanocomposites. **D**. EPR spectra of PVDF-Fe_3O_4 nanocomposites

regions 400 to 1400 cm^{-1} and 2000 to 4000 cm^{-1} are shown in Fig. 13B, C, respectively. The estimated locations of the lines originating from the polymer are represented by narrow blue rectangles, while narrow red rectangles indicate the positions of the predicted FTIR lines of the nanofiller. A vertical combination of blue and red (top) narrow rectangle reflects an overlap between the FTIR lines of the polymeric matrix and the nanofiller. The width of these rectangles is proportional to the experimental errors and may include the convolution of near lines. However, interactions between PVDF and Fe_3O_4 may generate a larger shift of the vibration lines, thus increasing the overlap of lines originating from different components. Such cases were not considered in this analysis.

The line located at 530 cm^{-1}, was reported as representing Fe-O vibrations in magnetite [36]. The line located at 565 cm^{-1} (or 580 cm^{-1} according to [34, 37]) was assigned to Fe-O stretching in highly crystalline Fe_3O_4 nanoparticles [38]. This line appears to be rather broad and weak, suggesting that the crystalline structure is distorted, in agreement with WAXS data, which indicate changes of the unit crystalline cells upon loading with the nanofiller. The line at 610 cm^{-1} was assigned to oxidized maghemite on the surface of magnetite [38]. Tentatively, the band located at 796 cm^{-1} was assigned to α-FeOOH [34], due to some humidify uptake. The band reported at 1620 cm^{-1}, attributed to bending vibrations originating from adsorbed water by the iron oxide nanoparticles [39], was not observed.

The line at 408 cm^{-1} was assigned to α PVDF obtained from solution at 60 °C [40]. As seen in Fig. 13B, this line decreases as the content of Fe_3O_4 increases. The vibration at 482 cm^{-1} was tentatively assigned to the γ or α phase of PVDF [41]. The vibration at 530 cm^{-1} was identified as CF_2 bending in the α PVDF [42]. The lines at 612 cm^{-1}, 760 cm^{-1} (766 cm^{-1} in [13]), 795 cm^{-1}, 853 cm^{-1}, and 974 cm^{-1} (976 cm-1 in [40]) were assigned to the α PVDF [12]. The recorded spectrum does not show the last two lines, which are either shifted by the interaction with the nanofiller or completely silenced (broadened). The line at 881 cm^{-1} if present is overlapping with the neighboring Fe_3O_4 line.

As noticed in Fig. 13B, many of the FTIR spectra in the range 400 to 1500 cm^{-1} are a superposition between Fe_3O_4 and PVDF lines. For such lines is impossible to analyze further the effect of the composition of the sample on the line's parameters (position, width).

Figure 13C collects the FTIR spectra in the range 2500 to 4000 cm^{-1}. These spectra are dominated by a doublet located near 3000 cm^{-1}, which may represent an interaction between the polymer and the nanofiller (or eventually hydrogen bond). A faint line located near 3800 cm^{-1} and assigned to the interaction between OH groups and iron nanoparticles may be noticed A doublet is noticed near 3000 cm^{-1} and assigned to the OH bonds [13].

EPR measurements in the X-band were performed; some spectra are collected in Fig. 13D. As expected, the polymeric matrix exhibits no resonance signal. The nanofiller [43] presents a signal similar to the PVDF composite loaded by 30% Fe_3O_4. The composites PVDF-Fe_3O_4 exhibit a strong resonance signal due to magnetically coupled Fe_3O_4 nanoparticles. As seen from Fig. 13D, the resonance signal is centered at external magnetic fields smaller than the magnetic field corresponding to the free electron ($g = 2.0023$), which is at approximatively 3400 Gs. This reflects the existence of a strong local magnetic field and indicated that the spectrometer was operating in the ferrimagnetic/ferromagnetic resonance mode (FMR) [30, 44, 45] correlated to the magnetic features of these nanocomposites. The width and the strength of the local magnetic field at resonance increased as the loading by Fe_3O_4 nanoparticles was increased. It is suggested that this reflects anisotropic electron interactions (among the electrons belonging to Fe^{3+} and Fe^{2+} states). The amount of information that can be extracted from the FMR lines of these nanocomposites is low because the magnetic nanoparticles are randomly oriented, averaging out the potential angular dependence of the FMR spectra [31, 45, 46].

Discussion

As seen in Fig. 14, the morphology of the nanocomposites under study is complex. The pristine polymer (PVDF) consists of crystalline islands (domains) dispersed within a continuous amorphous polymeric phase. The degree of crystallinity of the pristine polymer was estimated by WAXS to be of the order of 70%. An interface provides the transition between the amorphous continuous phase of PVDF and the crystalline domains of PVDF. The Fe_3O_4 nanoparticles are nanograins, consisting of several smaller crystallites. The nanoparticles are preferentially accommodated within the amorphous domains of the polymer or within the amorphous polymer-crystalline polymer interface. An additional interface may provide eventually the transition between the Fe_3O_4 nanoparticle and the amorphous polymeric phase. This is a result of the fact that the amorphous phase has a lower density than the crystalline one; consequently, at least at low loading with Fe_3O_4, the nanofiller will be embedded within the amorphous phase without significant distortion of the polymeric matrix (i.e. with negligible strain), as eventually, the amorphization of some crystallites (even partial) may provide additionally available volume fore the nanofiller.

The detailed analysis of the WAXS spectrum indicated that the linewidth of the crystalline polymeric phase of

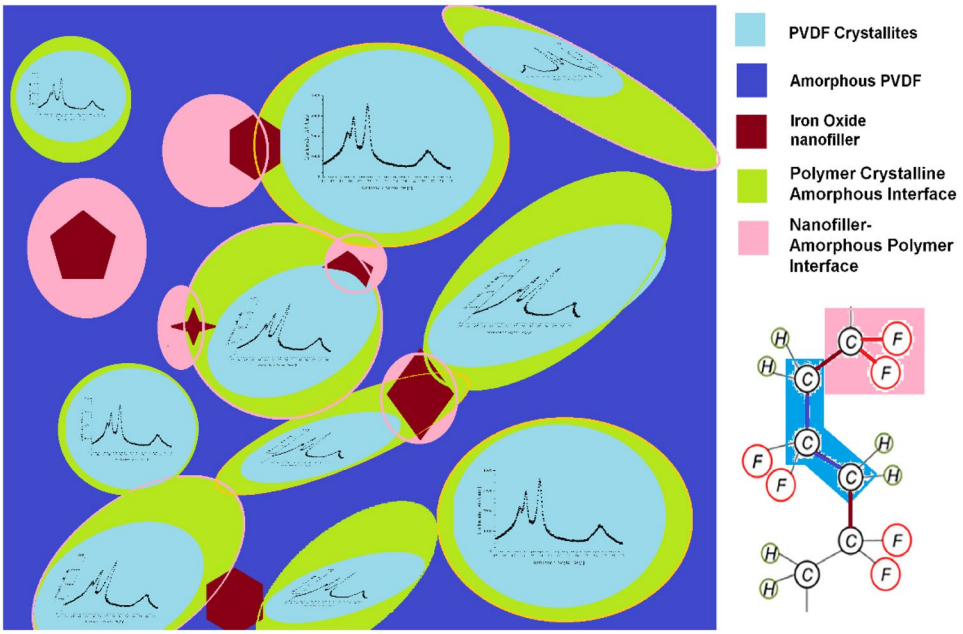

Fig. 14 Main phases of PVDF-Fe_3O_4 nanocomposites

PVDF-Fe_3O_4 nanocomposite is controlled by the size of polymeric crystallites, with the strain contribution becoming dominant for loading with nanoparticles greater than 12% wt. (see Fig. 8). Several regimes may be noticed:

1. The isostress regime occurs at very low loading with nanofiller (typically below 2.5% Fe_3O_4). For such low concentrations of the nanofiller, the degree of crystallinity is practically oscillating about 67%, due to the competition between several processes: As the concentration of the nanofiller is increased, the residual stress favors the shrinking of the size of the unit crystalline cell (for the polymer) while the (Scherrer) crystallites' size is increased, and Wilson's strain is decreased. The weak increase of the crystallites size may reflect a weak crystallization under stress. This is reflected in the WAXS experiment by the decrease of the line width and by the shits in the positions of WAXS lines, respectively. The slight decrease of the unit cell dimension and increase in the size of crystallites may reflect the fact that the conversion of some amorphous regions into crystalline domains generated additional volume capable of accommodating the nanofiller. The above-mentioned modifications are weak. Due to the elasticity of the polymeric matrix, the nanofiller is accommodated without generating significant stress. The low contribution of Wilson's strain supports this interpretation. While some modifications of the size of the unit crystalline size were noticed, owing to the low strains involved it appears natural to assume that within this range of concentration, the stress may be assumed almost constant and eventually negligible.
2. The linear elastic regime (between 2.5% and 5.0%wt. Fe_3O_4). Within this domain, the degree of crystallinity oscillates about 67%. In this range of concentration, the size of the unit crystalline cell is increased as the loading is increased. For most PVDF reflections, the Scherrer size of crystallites decreases slowly as the loading by Fe_3O_4 is increased. This reflects the fact that the pressure exerted by nanoparticles of crystallites became sufficiently strong to start breaking these crystallites. Additionally, some new crystallites are generated by crystallization under stress balancing the overall degree of crystallinity. At higher concentrations of nanofiller, the amorphous polymeric matrix is no more able to elastically accommodate more nanoparticles without strain build-up. Hence as the loading with nanoparticles is increased both the strain and the stress are increasing while typically remaining in the linear elastic range
3. In the range 5.0 to 15% wt. Fe_3O_4 a strong decrease in the degree of crystallinity was noticed as the concentration of the nanofiller was increased. In this range, the size of the crystalline unit cell was not significantly modified, the (Scherrer) crystallites size is slowly decreasing as the loading is increased, and the Wilson strain is increased as the loading with nanofiller was increased. This indicates that if the destruction of the crystallite starts, it will continue up to its complete disappearance, suggesting that destruction is dominant over the shrinking of crystallites.
4. The bleeding regime, for concentrations above 15% wt. Fe_3O_4. In this domain of Fe_3O_4 concentrations, the degree of crystallinity showed a weak decrease as the loading by Fe_3O_4 was increased. The size of the Scherrer

crystalline size decreased as the loading with the nanofiller was increased. A competition between crystallites shrinking and destruction was noticed. The amorphous polymeric phase was eventually broken, some of the nanofiller is released from the polymer and the parameters of WAXS and Raman spectra become almost independent of the loading with the nanofiller as the local stresses are relieved.

Conclusions

Spectroscopic (WAXS, Raman, and EPR) investigations on PVDF-Fe_3O_4 nanocomposites have been reported. WAXS, Raman, and FTIR data indicated that the pristine PVDF, as well as the polymeric phase of the PVDF-Fe_3O_4 nanocomposite, contains solely the alpha phase (within experimental errors). The presence of Fe_3O_4 nanoparticles was supported by WAXS, Raman, FTI, and EPR measurements.

A conversion from the α phase PVDF to β phase PVDF was reported and assigned to the loading by Fe_3O_4 nanoparticles (see Fig. 2b of [12]), increased mechanical stresses, and/or high-temperature treatments. Although the processing of these samples aimed at all these processes that should increase the β phase, no experimental data that support this phase was observed.

WAXS investigations revealed a complex modification of the line positions and line widths, suggesting a strong interaction between the matrix and the nanofiller. It was concluded that for loading with nanoparticles below 12% wt., the line width of the WAXS lines originating from polymeric crystallites is controlled by the size of crystallites. Larger concentrations of nanofiller start to generate significant strains/stresses, and for loadings with nanoparticles above 12% wt., strain/stress takes control over the line width.

To conclude, it was observed that for loading with Fe_3O_4 below 12% wt., the WAXS spectra obey with a good approximation the scenario 1, with the size of the polymeric crystallites dominating the WAXS spectra. A transition from regime one towards regime four starts as the content of nanofiller exceeds 5% wt. Fe_3O_4. As the amorphous phase is torn and eventually some nanoparticles are bleeding, the nanocomposite degenerates into two almost independent components (the polymer and the nanofiller). The manuscript describes for the first time the competition between destruction and shrinking of crystallites, based on a detailed analysis of WAXS data.

Raman spectroscopy supported WAXS data, revealing individual elastic behavior for different Raman lines (and corresponding molecular vibrations). Several regimes describing the main features of these nanocomposites as a function of Fe_3O_4 loading have been identified and discussed in the previous paragraph.

Raman data and partially FTIR investigations provided a molecular picture of the elastic features in these nanocomposites, with emphasis on the effect of nanofiller on elastic features, as revealed by the changes reported in the section focused on Raman and FTIR spectra. It is concluded that the nanofiller silenced the molecular vibrations of the polymeric matrix. This behavior was stronger in the case of Raman spectra, probably as the dipole moments of the α phase are compensated, resulting in less sensitive FTIR spectra (than Raman).

Acknowledgements This work was supported by grants from the Department of Defense W911NF-15-1-0063 (Raman), W911NF-19-1-0473 (EPR spectrometer), and NSF DMR 2122178 (URGV-UMN PREM)

Author contribution Each author contributed to the manuscript. All authors contributed to the manuscript. Dorina M. Chipara concentrated on Raman analysis of experimental data. Alexandro Trevino was responsible for the ESR spectra and contributed together with Bryan Hoke to the analysis of X-Ray data. Karen Lozano was in charge with the melt mixing of the polymer with the nanofiller to obtain a homogeneous nanocomposite. Bryan Hooke focused on X-Ray data collection and analysis. Karen S. Martirosyan contribution was focused on magnetic nanofiller and manuscript's design. Mircea Chipara focused on data simulation and analysis.

Funding The funding for this research originated from the following sources (also listed in the acknowledgments section of the manuscript).

Availability of data and material Data may be available upon request. The submitted document (Word version) includes the links required to access the graphs and the data contained in each graph. This link may be destroyed during the conversion of the Word file to the pdf version or final journal page type. Upon reasonable request, the authors may provide either the original data files or the original word document with active Origin links. An Origin viewer is required to access the data.

Code availability Data were processed using Origin Pro by exploiting the C Programming capabilities. The mathematical expressions for the simulations are included in the manuscript.

Declarations

Conflicts of interest The corresponding author declares on behalf of all authors that there is not any conflict and/or competing interest of any author that contributed to this manuscript.

References

1. Ceccorulli G, Pizzoli M, Scandola M, Alfonso GC, Turturro A (1989) Dynamic mechanical relaxations of poly(vinylidene fluoride)-poly(vinylpyrrolidone) blends. Polymer (Guildf) 30:1251–1256. https://doi.org/10.1016/0032-3861(89)90044-X
2. Linares A, Acosta JL (1997) Tensile and dynamic mechanical behaviour of polymer blends based on PVDF. Eur Polym J 33:467–473. https://doi.org/10.1016/S0014-3057(96)00182-6
3. Linares A, Acosta JL (1996) Dynamic mechanical properties of binary and ternary blends based on PVDF. Polym Bull 36:241–247. https://doi.org/10.1007/BF00294913

4. Koseki Y, Aimi K, Ando S (2012) Crystalline structure and molecular mobility of PVDF chains in PVDF / PMMA blend films analyzed by solid-state 19F MAS NMR spectroscopy. Polym J 44:757–763. https://doi.org/10.1038/pj.2012.76
5. Ma W, Zhang J, Chen S, Wang X (2008) Crystalline phase formation of poly(vinylidene fluoride) from tetrahydrofuran/N, N-dimethylformamide mixed solutions. J Macromol Sci Part B Phys 47:434–449. https://doi.org/10.1080/00222340801954811
6. Wu CM, Chou MH (2016) Polymorphism, piezoelectricity and sound absorption of electrospun PVDF membranes with and without carbon nanotubes. Compos Sci Technol 127:127–133
7. Constantino CJL, Job AE, Simões RD, Giacometti JA, Zucolotto V, Oliveira ON, Gozzi G, Chinaglia DL (2005) Phase transition in poly(vinylidene fluoride) investigated with micro-Raman spectroscopy. Appl Spectrosc 59:275–279. https://doi.org/10.1366/0003702053585336
8. Kobayashi M, Tashiro K, Tadokoro H (1975) Molecular vibrations of three Crystal forms of poly(vinylidene fluoride). Macromolecules 8:158–171. https://doi.org/10.1021/ma60044a013
9. Pradhan SK, Kumar A, Sinha AN, Kour P, Pandey R, Kumar P, Kar M (2017) Study of ferroelectric properties on PVDF-PZT nanocomposite. Ferroelectrics 516:18–27. https://doi.org/10.1080/00150193.2017.1362243
10. Gebrekrstos A, Madras G, Bose S (2018) Piezoelectric response in electrospun poly(vinylidene fluoride) fibers containing fluoro-doped graphene derivatives. ACS Omega 3:5317–5326. https://doi.org/10.1021/acsomega.8b00237
11. Kochervinskiĭ VV (2003) Piezoelectricity in crystallizing ferroelectric polymers: Poly(vinylidene fluoride) and its copolymers (a review). Crystallogr Rep 48:649–675. https://doi.org/10.1134/1.1595194
12. Tsonos C, Pandis C, Soin N, Sakellari D, Myrovali E, Kripotou S, Kanapitsas A, Siores E (2015) Multifunctional nanocomposites of poly(vinylidene fluoride) reinforced by carbon nanotubes and magnetite nanoparticles. Express Polym Lett 9:1104–1118. https://doi.org/10.3144/expresspolymlett.2015.99
13. Samadi A, Ahmadi R, Hosseini SM (2019) Influence of TiO2-Fe3O4-MWCNT hybrid nanotubes on piezoelectric and electromagnetic wave absorption properties of electrospun PVDF nanocomposites. Org Electron 75:105405. https://doi.org/10.1016/j.orgel.2019.105405
14. Lin Y, Zhang Y, Zhang F, Zhang M, Li D, Deng G, Guan L, Dong M (2021) Studies on the electrostatic effects of stretched PVDF films and nanofibers, Nanoscale Res Lett 16. https://doi.org/10.1186/s11671-021-03536-9
15. Kolonelou E, Loupou E, Klonos PA, Sakellis E, Valadorou D, Kyritsis A, Papathanassiou AN (2021) Thermal and electrical characterization of poly(vinyl)alcohol)/poly(vinylidene fluoride) blends reinforced with nano-graphene platelets. Polymer (Guildf) 224:123731. https://doi.org/10.1016/j.polymer.2021.123731
16. Kabir E, Khatun M, Nasrin L, Raihan MJ, Rahman M (2017) Pure β-phase formation in polyvinylidene fluoride (PVDF)-carbon nanotube composites. J Phys D Appl Phys 50:aa5f85. https://doi.org/10.1088/1361-6463/aa5f85
17. Tjong SC, Chen H (2004) Nanocrystalline materials and coatings. Mater Sci Eng R Rep 45:1–88. https://doi.org/10.1016/j.mser.2004.07.001
18. Chipara DM, Panaitescu DM, Lozano K, Gabor RA, Nicolae CA, Chipara M (2019) Raman spectroscopy and molecular bases of elasticity: SEBS-graphite composites. Polymer (Guildf) 176:74–88. https://doi.org/10.1016/j.polymer.2019.05.019
19. Avanzini L, Brambilla L, Marano C, Milani A (2017) Strain-dependent vibrational spectra and elastic modulus of poly(p-phenylene terephtalamide) from first-principles calculations. Polymer (Guildf) 116:133–142. https://doi.org/10.1016/j.polymer.2017.03.073
20. Lei Z, Wang Y, Qin F, Qiu W, Bai R, Chen X, Lei Z, Wang Y, Qin F, Qiu W, Bai R, Chen X (2016) Multi-fiber strains measured by micro-Raman spectroscopy principles and experiment. Opt Lasers Eng 77:8–17
21. Ali N, Chipara D, Lozano K, Hinthorne J, Chipara M (2017) Polyethylene oxide—fullerene nanocomposites. Appl Surf Sci 421:220–227. https://doi.org/10.1016/j.apsusc.2016.11.166
22. Chipara D, Kuncser V, Lozano K, Alcoutlabi M, Ibrahim E, Chipara M (2020) Spectroscopic investigations on PVDF-Fe2O3 nanocomposites. J Appl Polym Sci 137:1–13. https://doi.org/10.1002/app.48907
23. Salimi A, Yousefi AA (2003) FTIR studies of β-phase crystal formation in stretched PVDF films. Polym Test 22:699–704. https://doi.org/10.1016/S0142-9418(03)00003-5
24. Gregorio R (2006) Determination of the α, β, and γ crystalline phases of poly(vinylidene fluoride) films prepared at different conditions. J Appl Polym Sci 100:3272–3279. https://doi.org/10.1002/app.23137
25. Jurczuk K, Galeski A, Mackey M, Hiltner A, Baer E (2015) Orientation of PVDF α and γ crystals in nanolayered films. Colloid Polym Sci 293:1289–1297. https://doi.org/10.1007/s00396-015-3542-7
26. Balzar D (1993) X-ray diffraction line broadening: modeling and applications to high-Tc superconductors. J Res Natl Inst Stand Technol 98:321. https://doi.org/10.6028/jres.098.026
27. Custódio FJMF, Steenbakkers RJA, Anderson PD, Peters GWM, Meijer HEH (2009) Model development and validation of crystallization behavior in injection molding prototype flows. Macromol Theory Simul 18:469–494. https://doi.org/10.1002/mats.200900016
28. Ariffin A, Ariff ZM, Jikan SS (2011) Evaluation on nonisothermal crystallization kinetics of polypropylene/kaolin composites by employing Dobreva and Kissinger methods. J Therm Anal Calorim 171–177. https://doi.org/10.1007/s10973-010-1013-4
29. Khanna YP, Kuhn WP (1997) Measurement of crystalline index in nylons by DSC. J Polym Sci Part B Polym Phys 1997:2219–2231. https://doi.org/10.1002/(SICI)1099-0488(199710)35:14%3c2219::AID-POLB3%3e3.0.CO;2-R
30. Muhammed Shafi P, Chandra Bose A (2015) Impact of crystalline defects and size on X-ray line broadening: a phenomenological approach for tetragonal SnO2 nanocrystals. AIP Adv 5. https://doi.org/10.1063/1.4921452
31. Sen SK, Barman UC, Manir MS, Mondal P (2020) X-ray peak profile analysis of pure and Dy-doped α-MoO 3 nanobelts using Halder-Wagner methods. Adv Nat Sci Nanosci Nanotechnol 11
32. Nath D, Singh F, Das R (2020) X-ray diffraction analysis by Williamson-Hall, Halder-Wagner and size-strain plot methods of CdSe nanoparticles - a comparative study. Mater Chem Phys 239:122021. https://doi.org/10.1016/j.matchemphys.2019.122021
33. Mote V, Purushotham Y, Dole B (2012) Williamson-Hall analysis in estimation of lattice strain in nanometer-sized ZnO particles. J Theor Appl Phys 6:2–9. https://doi.org/10.1186/2251-7235-6-6
34. Ni S, Wang X, Zhou G, Yang F, Wang J, Wang Q, He D (2009) Hydrothermal synthesis of Fe3O4 nanoparticles and its application in lithium ion battery. Mater Lett 63:2701–2703. https://doi.org/10.1016/j.matlet.2009.09.047
35. Chapron D, Rault F, Talbourdet A, Lemort G, Cochrane C, Bourson P, Devaux E, Campagne C (2021) In-situ Raman monitoring of the poly(vinylidene fluoride) crystalline structure during a melt-spinning process. J Raman Spectrosc 1–7. https://doi.org/10.1002/jrs.6081
36. Mahdavi M, Ahmad MB, Haron MJ, Namvar F, Nadi B, Rahman MZA, Amin J (2013) Synthesis, surface modification and characterisation of biocompatible magnetic iron oxide nanoparticles for biomedical applications. Molecules 18:7533–7548. https://doi.org/10.3390/molecules18077533
37. Wei S, Zhu Y, Zhang Y, Xu J (2006) Preparation and characterization of hyperbranched aromatic polyamides/Fe3O4 magnetic

nanocomposite. React Funct Polym 66:1272–1277. https://doi.org/10.1016/j.reactfunctpolym.2006.03.008
38. Rasouli E, Basirun WJ, Rezayi M, Shameli K, Nourmohammadi E, Khandanlou R, Izadiyan Z, Sarkarizi HK (2018) Ultrasmall superparamagnetic Fe 3 O 4 nanoparticles: Honey-based green and facile synthesis and in vitro viability assay. Int J Nanomedicine 13:6903–6911. https://doi.org/10.2147/IJN.S158083
39. Shagholani H, Ghoreishi SM, Mousazadeh M (2015) Improvement of interaction between PVA and chitosan via magnetite nanoparticles for drug delivery application. Int J Biol Macromol 78:130–136. https://doi.org/10.1016/j.ijbiomac.2015.02.042
40. Yang L, Qiu J, Shao B, Zhu K, Ji H (2012) Effect of temperature on the crystalline phase, dielectric properties of poly (vinylidene fluoride) (PVDF) film 23rd. Int Conf Adapt Struct Technol ICAST 2012(4):4489–4500
41. Cai X, Lei T, Sun D, Lin L (2017) A critical analysis of the α, β and γ phases in poly(vinylidene fluoride) using FTIR. RSC Adv 7:15382–15389. https://doi.org/10.1039/c7ra01267e
42. Bormashenko Y, Pogreb R, Stanevsky O, Bormashenko E (2004) Vibrational spectrum of PVDF and its interpretation. Polym Test 23:791–796. https://doi.org/10.1016/j.polymertesting.2004.04.001
43. Annveer AK, Ritu MC, Pant RP (2015) A Review on WO3 films prepared by various methods. Appl Sci Lett 1:115–124. https://doi.org/10.17571/appslett.2015.01026
44. Owens FJ (2003) Ferromagnetic resonance of magnetic field oriented Fe3O 4 nanoparticles in frozen ferrofluids. J Phys Chem Solids 64:2289–2292. https://doi.org/10.1016/S0022-3697(03)00261-0
45. Aktas B (1997) FMR properties of epitaxial Fe3O4 films on MgO(100). Thin Solid Films 307:250–259. https://doi.org/10.1016/S0040-6090(97)00311-8
46. Ali N, Chipara M, Balascuta S, Skomski R, Sellmyer DJJ (2008) Ferromagnetic resonance investigations on styrene-butadiene-styrene barium ferrite nanocomposites. J Nanosci Nanotechnol 8:1–5. https://doi.org/10.1166/jnn.2008.S315